

# Cascadia Daily GNSS Time Series Denoising: Graph Neural Network and Stack Filtering

L. Bachelot <sup>1</sup>, A. M. Thomas <sup>1,2</sup>, D. Melgar <sup>1</sup>, J. Searcy <sup>3</sup>, Y-S. Sun <sup>1</sup>

<sup>1</sup>Department of Earth Sciences, University of Oregon, Eugene, OR, USA, <sup>2</sup>Department of Earth and Planetary Sciences, University of California, Davis, CA, USA, <sup>3</sup>School of Computer and Data Sciences, University of Oregon, Eugene, OR, USA

**Author contributions:** *Conceptualization:* L. B., A. M. T., D. M. *Data Curation:* L. B. *Formal Analysis:* L. B., A. M. T., D. M. *Funding Acquisition:* A. M. T., D. M. *Investigation:* All authors. *Methodology:* L. B., A. M. T., D. M., J. S. *Project Administration:* A. M. T., D. M. *Resources:* L. B., A. M. T., D. M., J. S. *Software:* L. B., A. M. T., D. M., J. S. *Supervision:* A. M. T., D. M. *Validation:* All authors. *Visualization:* L. B. *Writing – original draft:* L. B., A. M. T., D. M. *Writing – review & editing:* All authors.

**Abstract** Precise Global Navigation Satellite System (GNSS) time series have greatly advanced tectonic studies, particularly in detecting transient deformation signals like slow slip events (SSEs). However, GNSS position data can be noisy, impacting the accuracy of analyses. Traditional denoising methods often struggle with spatially heterogeneous and evolving networks. This study introduces a novel Graph Neural Network (GNN) approach to denoise GNSS time series, effectively managing network heterogeneity and varying station availability. GNNs are robust against temporal gaps, making them suitable for GNSS data. Applied to daily time series for the Cascadia Region processed by the University of Nevada Reno and Central Washington University, our method reduced common-mode noise by more than 70% and 30% on horizontal components, in the two datasets respectively, significantly enhancing surface displacement measurements and slow slip events (SSE) source property estimation. We compared the GNN approach with three simple stack filtering methods, which performed comparably in many situations but are more sensitive to parameter choices. For all methods, substantial noise reduction removes artifacts that could impact geophysical interpretations. Our findings suggest that GNN-based denoising offers a robust, adaptive solution for heterogeneous GNSS networks, enhancing accuracy in tectonic and volcanic process studies, but stack filtering approaches might still outperform the machine learning technique depending on the application.

Production Editor:  
Christie Rowe  
Handling Editor:  
Jonathan Weiss  
Copy & Layout Editor:  
Hannah F. Mark

Signed reviewer(s):  
Hongyu Sun  
Walter Szeliga

Received:  
October 24, 2024  
Accepted:  
March 1, 2025  
Published:  
March 23, 2025

**Non-technical summary** GNSS are satellite-based systems used for precise positioning and navigation on Earth. They include systems like GPS (United States), GLONASS (Russia), Galileo (Europe), and others. In earth science, GNSS antennas are used to monitor Earth's crustal deformations such as tectonic movements and earthquakes or, in this study, slow slip events (SSEs). SSEs are a type of tectonic movement where the Earth's tectonic plates move slowly over days to months, rather than quickly as in earthquakes. The subtle movements during SSEs (maximum of around 1cm) are challenging to detect because they require extremely precise measurements, and even small errors in GNSS data can lead to significant inaccuracies and biases in analyzing these events. A GNN is effective for cleaning GNSS data because it can identify and eliminate noise that affects multiple stations in a network by understanding the relationships between them. Using GNN on daily GNSS data, we reduced correlated noise by 70% in the University of Nevada Reno dataset and by 30% in the Central Washington University dataset. The added precision allows us to more accurately detect and analyze SSEs, leading to a better understanding of these phenomena.

## 1 Introduction

The Global Navigation Satellite System (GNSS) is a group of several constellations of satellites that provides signals enabling precise positioning and navigation on Earth. GNSS is used in a variety of Earth science applications (e.g., reviews in Bock and Melgar, 2016; Larson, 2019) and it offers high-precision (cm to mm level) time series data that allows researchers to monitor subtle movements in the Earth's crust (Geng et al., 2018; Bertiger et al., 2020). It is often used to identify deformation transients (e.g. Szeliga et al., 2008; Nishimura et al., 2013; Wallace, 2020), estimate tectonic plate motions (Prawirodirdjo and Bock, 2004; DeMets et al., 2010; Kreemer et al., 2014), detect and characterize large earthquakes (e.g. Lin et al., 2021; Goldberg and Haynie,

2022) and estimate seismic hazards (Moreno et al., 2011; Rollins et al., 2018; Rollins and Avouac, 2019; Meade and Hager, 2005).

Of particular interest to seismology and tectonics are slow slip events (SSEs) which are episodes of slip on a fault at much slower rupture and slip speeds and longer durations than typical earthquakes of the same size (Bürgmann, 2018). They have only very weak seismic radiation (or none at all) and, hence, GNSS is the primary tool used to study their resultant crustal deformation signals. SSEs have been detected in many subduction zones around the world (e.g., Jolivet and Frank, 2020), and in this work, we will focus on SSEs in the Cascadia Subduction Zone (CSZ). Here, SSEs occur between 20 and 40 km depth, downdip of the seismogenic zone (e.g., Bartlow, 2020), and do not occur uniformly along

the entire length of the margin. There is significant along-strike variability in their spatial extents, recurrence intervals, and source properties that are linked to variations in the structure of the overriding plate (Delph et al., 2021). In GNSS data, SSEs manifest as transient reversals in the direction of secular motion expected from plate tectonic motion on multiple nearby stations (Miller et al., 2002; Bartlow et al., 2011; Wang et al., 2001; Rogers and Dragert, 2003). Identification of SSEs in GNSS time series can be challenging because even large SSEs produce only very small (i.e. few mm to cm) magnitude surface displacements. Such displacements are difficult to identify in daily data and even more so in high-rate data which have higher noise amplitude (Geng et al., 2018; Melgar et al., 2020).

Despite over 20 years of research, our understanding of the underlying mechanism or mechanisms responsible for SSEs is still evolving. GNSS noise level is often of the same order of magnitude as the signal of interest (2–8 mm). If we could lower GNSS displacement noise levels such that we could resolve subtle signals in both daily and sub-daily sampling GNSS data, it would undoubtedly improve our understanding of the phenomenon. For example, identification of the exact onset of the phenomena is currently challenging because of this elevated noise. Likewise, being able to measure smaller magnitude SSEs would facilitate better understanding of the magnitude-frequency distribution, scaling properties, spatial distribution, and triggering mechanisms of SSEs which are sensitive to small magnitude stress changes such as those from Earth tides (e.g., Royer et al., 2015). High-rate GNSS can also be used to assess the detailed evolution of slip in space and time (Itoh et al., 2022). Analysis of high-resolution seismicity catalogs elucidate coherent seismicity migration patterns that are distinct from the main slip front. These secondary fronts are inferred to be smaller scale slip events that propagate at different speeds and directions and collectively contribute to the total slip in SSEs (Ghosh et al., 2010; Houston et al., 2011; Rubin and Armbruster, 2013; Peng et al., 2015; Royer et al., 2015; Bletery et al., 2017). Identifying these fronts in high-rate GNSS data would permit slip inversions and estimates of properties such as stress drops that are important for assessing the dynamics of SSEs. These could complement estimates of the same properties derived from other geophysical observations (e.g., Hawthorne et al., 2016). Finally, higher resolution GNSS displacements (i.e. there is lower overall noise) could be used to identify precursory transient deformation which is thought to have preceded multiple large magnitude earthquakes (e.g., Kato et al., 2012; Ito et al., 2013; Ruiz et al., 2014; Socquet et al., 2017).

Lowering GNSS noise levels has been challenging because position calculations are susceptible to various sources of noise that can impact their accuracy. These include atmospheric contributions to noise from the ionosphere, troposphere, and local and regional weather conditions (Wu et al., 2013; Hadas et al., 2013; Lu et al., 2016). Additionally, satellite-related factors like orbit variations and clock offsets contribute to the overall noise in significant ways (e.g., Kazmierski et al.,

2020). Station specific issues, including static and clock offsets, further compound the challenges. The noise can be high frequency and particular to a single station (white or colored noise) or correlated across multiple stations (common mode noise or error) depending on the source. The challenge of positioning algorithms is to account for most of these noise sources while solving an optimization problem to obtain a particular station's time-varying coordinates (Herring et al., 2016; Geng et al., 2019; Bertiger et al., 2020). This results in a time series of positions of varying sample rates which typically range from daily to sub-daily. However, the combination of approximations from individual sources introduces complexity, making it challenging to effectively utilize estimates of ionospheric activity, tropospheric water vapor, or other data as inputs for denoising algorithms due to the loss of correlation between the direct sources of noise and the resulting position time series.

Common mode noise (or common mode error) manifests as displacement with magnitude and direction that is correlated in space across distances greater than the natural signals (e.g. SSEs) we study on similar time scales (Figure 1). Various methods have been proposed to reduce common mode noise. The simplest, known as stack filtering (Wdowinski et al., 1997; Nikolaidis, 2002) was one of earliest adopted approaches and it is applied to small regions within a fixed network, with the goal of highlighting the differences between the stations. Several additional, more complex approaches have also been proposed. For example, He et al. (2015) uses a Principal Component Analysis (PCA) to identify the correlations across stations to remove them. In our case, this would lead to removing the signal as SSE is highly correlated across stations. The same issue is valid for the Karhunen–Loeve expansion method proposed by Dong et al. (2006). Often these methods are used effectively to highlight differences between stations in the same network but not to look at absolute displacement for an event. Wavelet transform (WT) approaches can also be used for GNSS signal denoising (Tao et al., 2021; Satirapod and Rizos, 2005; Azarbad and Mosavi, 2013). By decomposing the signal, it is then possible to eliminate the noise. However, distinguishing the noise from the decomposed signal is difficult, and therefore wavelets are mostly used to remove single-station high-frequency noise and not for common mode noise. Combining the advantages of PCA and WT for denoising GNSS data, Li et al. (2017) introduced a WT-based multiscale multiway PCA. Many other methods based on signal decomposition and PCA to denoise daily GNSS and high-rate GNSS exist as well (Li et al., 2021, 2023). In recent years, machine learning has been applied to remove noise in different domains using U-Net types of networks (Ronneberger et al., 2015). U-Nets have been applied in seismology with Deep Denoiser (Zhu et al., 2019), and more recently on high-rate GNSS data (Thomas et al., 2023). While U-Nets have proved successful in removing single station noise, they do not leverage network information.

Graph Neural Networks (GNNs, Kipf and Welling, 2017) are a type of artificial neural network capable of leveraging spatial information based on graph-

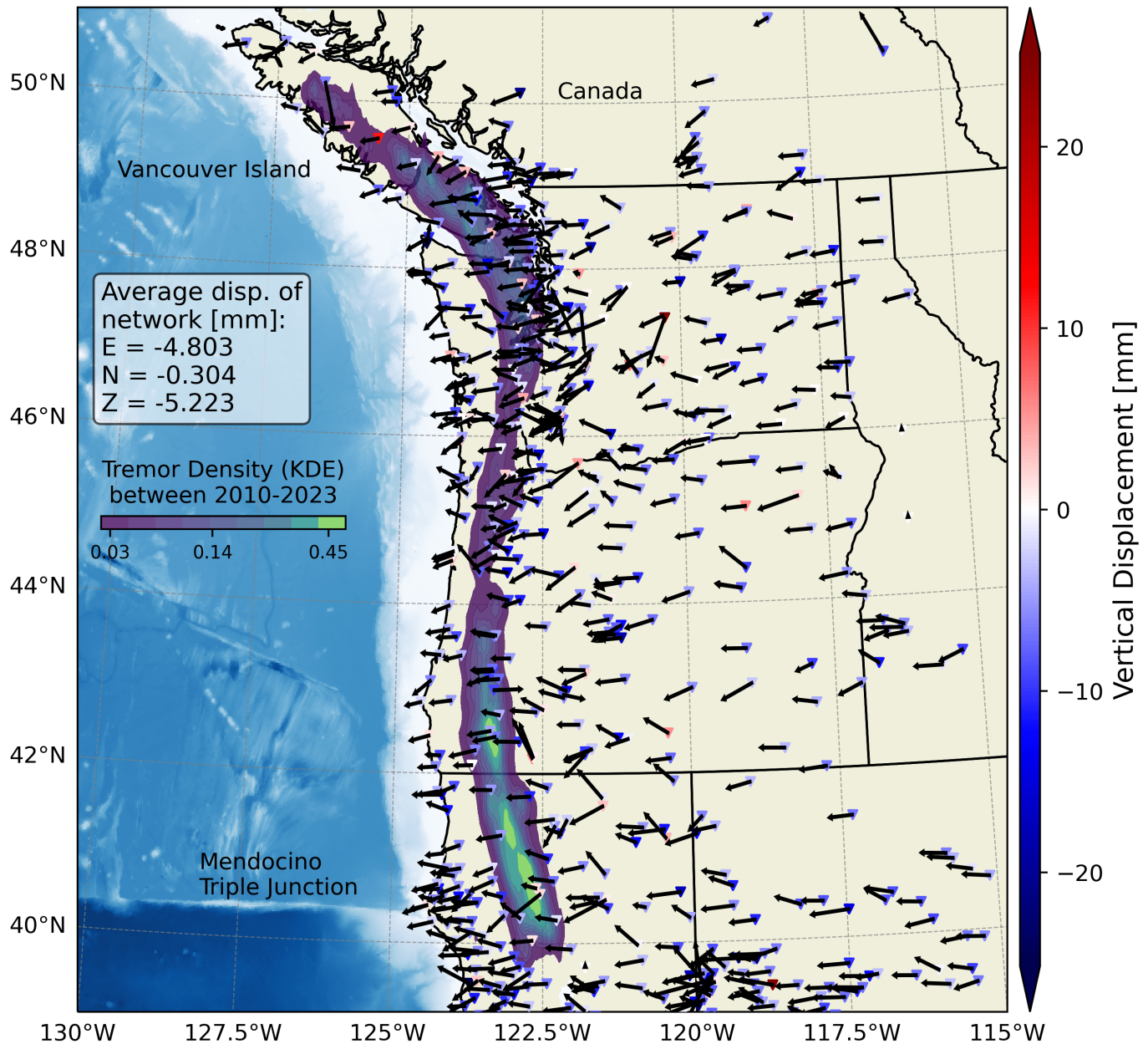


**Figure 1** Daily displacements recorded on Cascadia GNSS stations on 2016-02-16. Stations are colored by the magnitude of the vertical displacement component. Common mode noise manifests as similar, spatially correlated offsets. This particular day is strongly affected by common mode noise; the average displacement is very high (-4.852 mm and -5.229 mm in the east and vertical directions respectively). We also highlighted the area where SSEs occurs with the tremor Kernel Density Estimation map for the full study period (2010-2023).

structured data. They rely on the same principles as the Convolutional Neural Network (CNN) (Lecun et al., 1998) and other deep learning methods (LeCun et al., 2015). GNNs utilize neighboring spatial information; however, while CNNs operate on a regularly sampled rectangular grid, GNNs can work on irregularly sampled data that has been structured as a graph (Kipf and Welling, 2017). GNNs can be used to make classifications or regressions at node, edge, or graph levels. The key component of the GNN is the message-passing layer, which enables nodes in a graph to update their representations by exchanging information with their neighbors (based on the edge connections). This enables the modeling of complex relationships and interdependences between nodes. In our case, the nodes are the GNSS

stations, and the edges are the inverse of the distance between them. This graph representation allows us to capture the heterogeneity of the spatial distribution of the network. The problem we are solving is a node-level regression. Shi et al. (2021) proposed a graph-masked label prediction approach to mix both graph node classification problems and graph label propagation to get maximum performances in predicting the labels at each node using the connected nodes (Shi et al., 2021). GNNs present a lot of advantages to processing GNSS data: The network geospatial structure is very important as nearby stations are more correlated.

GNNs are flexible in terms of the number of nodes, enabling seamless incorporation of new stations into the network allowing for efficient learning and adap-

tation without requiring any changes. Similarly, when stations are decommissioned or undergo significant changes, the flexibility in node management enables the GNN to handle these alterations. GNNs also keep the same advantages as more classic neural networks in dealing with missing data and robustness. This flexibility in the graph construction also allows us to control how the nodes are linked together to constrain the predictions to only the noise by excluding nearby information, which is impossible to do with a PCA-based denoising method, for example. GNNs have already proven successful in various seismology applications ([Zhang et al., 2022](#); [van den Ende and Ampuero, 2020](#); [Bloemheuvel et al., 2022](#); [McBrearty and Beroza, 2023](#)).

In this work, we apply a GNN approach to denoise GNSS displacement records in Cascadia. We focus on common mode noise by leveraging its spatial correlation across greater distances than the signals of interest to remove it from the original signal. To implement this concept in a GNN framework, we utilize connections between nodes in the GNN (i.e., the GNSS stations) over large distances, where the spatial correlation of Earth signals of interest is small or nonexistent. Figure 2 is a schematic diagram describing our denoising approach. Figure 2a shows the target station that records both an ongoing SSE and common mode noise. The connected stations used for prediction (input stations) are not expected to record displacements from the SSE but still record common mode noise. Therefore, careful consideration of the connections is crucial to ensure the GNN predicts noise and no signal of interest (more details in Section 2.3). The GNN model tries to predict the original signal at the target station using information from the input stations. This prediction is considered to be noise and is then removed from the original signal, leaving only the underlying signal of interest. In the schematic in Figure 2, the original signal contains both an offset from an ongoing SSE and strong common mode noise (Figure 2b). This offset (negative slope) is not present in the input stations signal (Figure 2c). We use the GNN to make a noise prediction at the target station; the result is shown in Figure 2d. This prediction is subtracted from the original signal, to produce the denoised data (Figure 2e). In this schematic, we highlighted with a red circle common mode noise through the processing. Common mode noise is present in the original signal (2b) at the target station, but also in the input stations (2c). This gets captured by the GNN and predicted as noise (2d) and then gets subtracted from the original signal (2e). This approach enhances the precision of GNSS data analysis by mitigating noise sources and isolating the relevant geodetic signals of interest (such as SSEs or other transients) for further scientific interpretation and investigation.

## 2 Methods

### 2.1 Data

We utilize data from two different processing centers: the University of Nevada Reno Geodetic Lab (UNR, [Blewitt et al., 2018](#)) and Central Washington University

(CWU, [Herring et al., 2016](#)). We download daily time series from all stations between longitudes -128.2°W and -115°W and latitudes 39°N and 51°W which extends from North Vancouver Island to the Mendocino Triple Junction and from the coast to ~500 km inland as can be seen in Figure 1. We initially restricted the area to between -128.2 and -120°W in longitude but including eastern stations better captures the regional noise characteristics. The stations to the east of the Cascades are also more stable (further from the plate boundary). We do not remove the stations on the volcanoes even if they are known to behave very differently than the rest. This allows us to validate the behavior of the GNN with stations that should not correlate with the rest of the network, resulting in a model that is more robust to station malfunctions or other unexpected behaviors. We consider the period between 2010 and 2023 to allow for comparison with the PNSN tremor catalog ([Wech, 2021](#)). The input data for the GNN is the time series recorded on the three components (North, East and vertical). We have considered adding other information such as site coordinates to help the network learn the specific characteristics of each site as suggested in [van den Ende and Ampuero \(2020\)](#). However, using more site-specific information as input also limits the network's ability to generalize. We want the GNN to be able to incorporate new stations without a gap in performance and having site specific information could make this more difficult.

### 2.2 Preprocessing

Before inputting data into the GNN, a data preprocessing pipeline is implemented. The first step involves detrending the time series data using a polynomial of first order (linear trend). This detrending process is conducted within maintenance segments, such as antenna changes, with a distinct polynomial fit for each station and the period between two maintenance intervals. The maintenance dates are recovered from the UNR website. Using the maintenance segments allows the removal of jumps in the time series. Following detrending, we remove outliers by applying a 99th percentile threshold on the detrended time series. This process effectively identifies and eliminates outliers, such as significant displacements exceeding 50 cm within a single day. Finally, the data is scaled between 1 and -1 using a min-max scaler, ensuring a standardized range for the input features.

### 2.3 Graph Construction

After the preprocessing and data cleaning, we construct the graphs through a series of steps. Initially, the data is partitioned into overlapping 30-day windows, with a substantial 90% overlap to ensure a continuous and comprehensive representation of temporal patterns. In this step, stations lacking more than 80% of the data within these windows are systematically removed from the graph. This removes stations that are not available at the specified time window. Determining edge length in the context of predicting correlated noise between nodes but preventing prediction of the signal of inter-

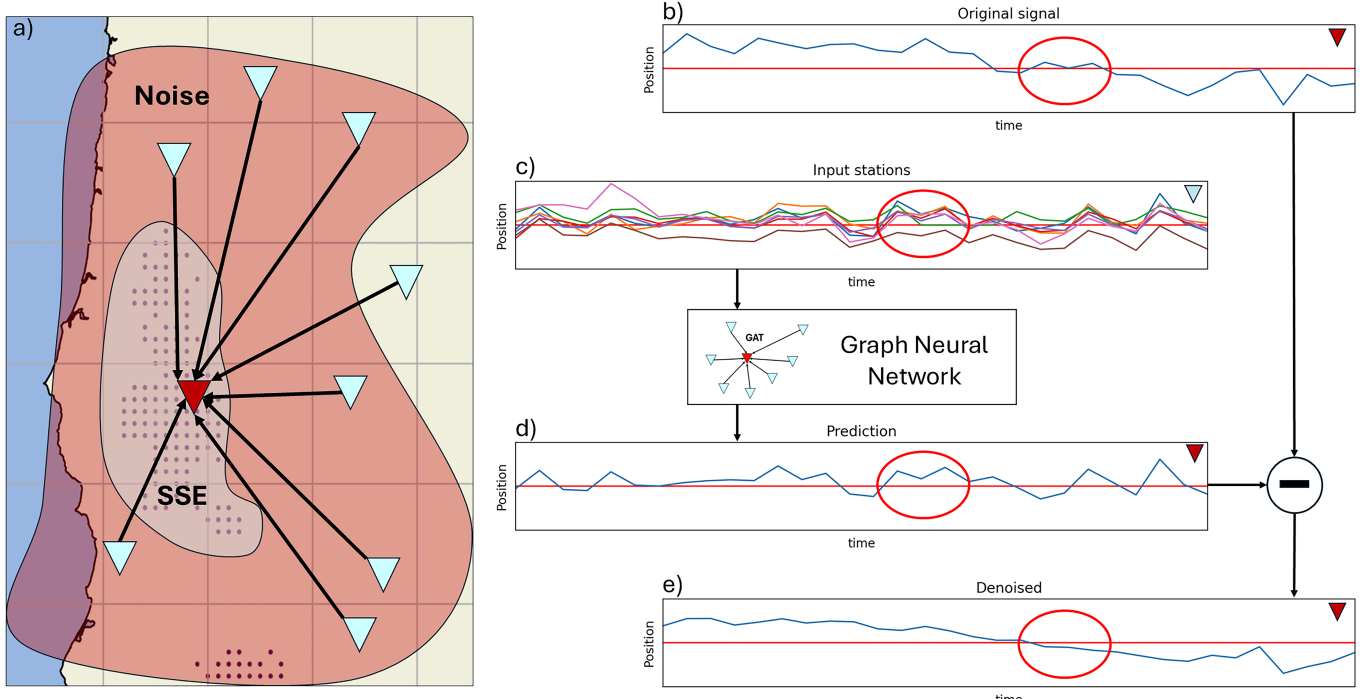


**Figure 2** Schematic example of denoising at one station (called a target station). (a) Map of the area and an example target station (in red) and the input stations (in blue). The target station is within a region expected to experience surface displacements owing to the SSE (represented with red dots in the background for tremors). While the input stations are outside of it. All the stations are affected by the same common mode noise. (b) Displacements recorded at the target station. The station is masked for the GNN so not used as input. (c) Displacements recorded on the input stations at the same time. (d) Noise prediction with the GNN at the target station. (e) Denoised signal at the target station. (i.e., GAT=Graph Attention Network, SSE=Slow Slip Event).

est proved challenging. We want the shortest edges possible to capture local noise, but we also need to prevent the prediction of displacements caused by SSEs. Through empirical testing of edge lengths, a distance of 400 km has been identified as shortest edge length after which we do not see any improvements in the SSE offset consistency metric (Section 2.7, and Figure 8), controlling how much signal of interest is removed. This is specific to our area of interest and the chosen time window. For periods longer than 30 days, or different geographic areas, SSEs might be detectable 400 km away and therefore the edge length needs to be greater. We apply a k-nearest neighbors clustering algorithm with this constraint (selecting the 8 nearest nodes with a distance greater than 400 km) to build the edges of the graphs. In other area/time windows, shorter edge lengths could be chosen to better remove more localized noise, both spatially and temporally. This graph construction methodology allows the resulting network to capture relevant spatial and temporal relationships between noise across the GNSS stations. Between January 1, 2010, and December 31, 2023, we generate 1695 graphs. The average number of stations per graph for the UNR dataset is 546.4, and 420.4 for the CWU.

## 2.4 Graph Neural Network Architecture

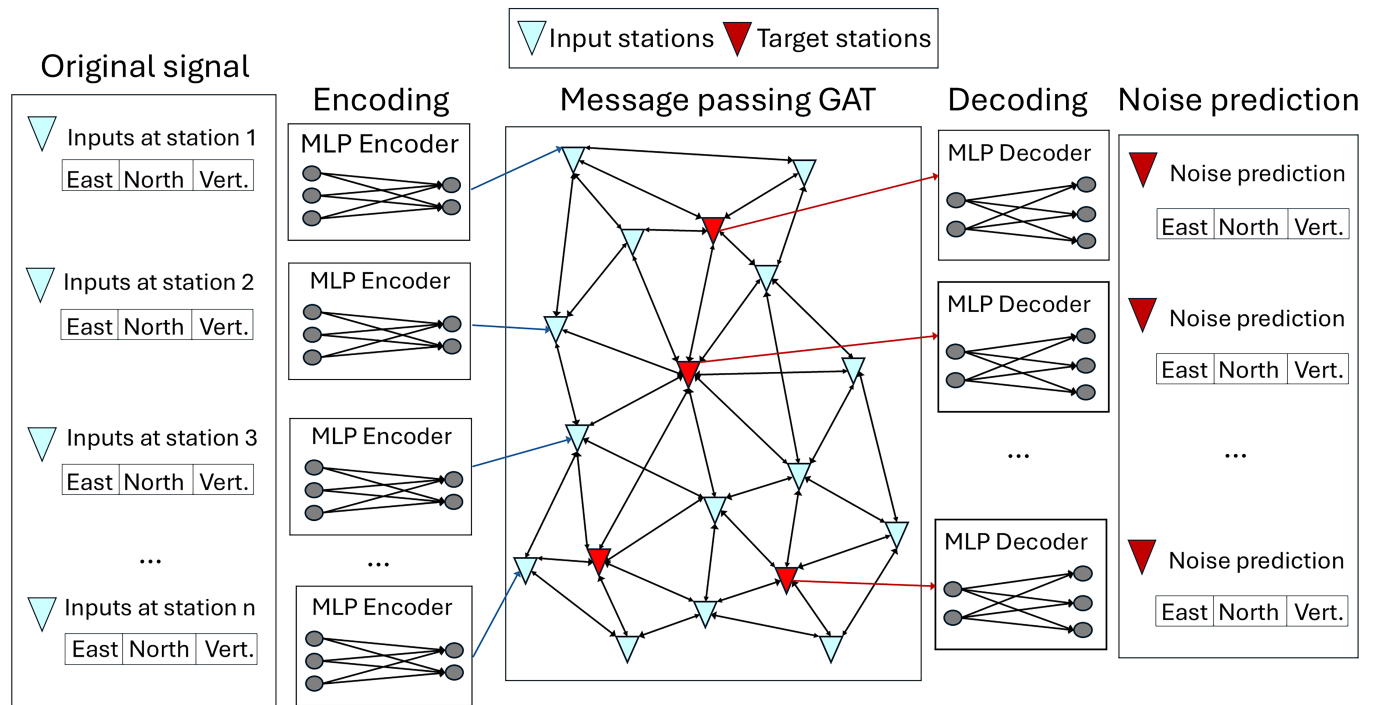
The GNN architecture for predicting noise is composed of 3 modules: feature extraction, spatial message passing, and noise reconstruction, shown schematically in

Figure 3. The initial stage is a Multi-Layer Perceptron (MLP) size 90-512-256 and rectified linear unit activation function (ReLU) for feature extraction, utilizing the signal data from the three components within a 30-day window as input. The same MLP with the same weights is applied to all the nodes. Then, the Graph Attention Network (GAT, Brody et al., 2021) layer is implemented with two attention heads for effective message passing among nodes. Notably, self-loops are excluded to prevent a station from seeing its own signal, forcing it to rely on the other nodes for prediction. Following the GAT layer, decoding is performed using an additional MLP of size 512-512-90, activation ReLu, and output linear designed to reconstruct the noise inherent in the GNSS data.

## 2.5 Training

During GNN training, we adhere to the following steps to ensure effective model learning and generalization. The dataset is split into training and test sets, with the years 2022 and 2023 reserved for testing purposes. Furthermore, to assess the model's performance during training, an 80% train/20% validation random split is employed for validation. Each training iteration involves processing batches of 64 graphs, where individual graphs within a batch are combined and treated as a single unit yet remain unconnected.

During the training process, dynamic random masks are created for each batch, selecting 30% of all nodes



**Figure 3** Architecture of the graph neural network. The inputs at all stations are the normalized signal on the three components. The neural network is divided into three parts: an MLP for signal encoding, then a GAT with 2 attention heads and no self-loop, and it finishes with another MLP for the signal decoding, reconstructing the noise prediction at all the stations. Here the representation does not account for the edge length constraint in the message passing panel.

(GNSS stations). The selected (masked) node inputs are then set to 0 (neutral value after normalization) for the 3 components East, North, and Vertical. This masking strategy is used to ensure the GAT is not learning and relying on the station itself to predict the noise but is using the neighboring stations. The absence of a self-loop prevents the direct use of the signal itself, but the attention mechanism could rely on the original signal to aggregate the inputs from neighboring nodes. It also introduces variability in the training data, encouraging the model to adapt to diverse scenarios as some stations set to 0 are also used as input. The forward step is then computed based on the masked graphs. The loss function employed is Mean Squared Error between the original signal at the masked station and the prediction, calculated exclusively on masked nodes. This approach guarantees that the model focuses on predicting and adjusting for the relevant nodes.

Subsequently, the training process iterates through batches, and the model learns iteratively from the masked nodes. Training continues until there is no further improvement in the validation loss, with a pre-defined patience of 50 epochs. This patience mechanism prevents premature termination, minimizes the risk of overfitting, and allows the model sufficient time to converge. Once the training concludes, the weights associated with the lowest validation loss are restored, ensuring the model retains the optimal configuration achieved during the training process.

## 2.6 Time Series Reconstruction

Once the training is complete, we take the following steps to produce the final time series. First, predictions are conducted on overlapping 30-day windows. We overlap by 90%, shifting by three days. This leads to ten different graphs over one time step, enabling the model to capture nuanced temporal dependencies. In this prediction step, we assume the model learned not to use the station itself to make the prediction. Therefore, we decided to not use masking and do the prediction for one time window in only one step, saving about 500 forward steps per time window if we were to mask and predict each station individually with masking. The SSE offset metric shows that the network is not relying on the station itself for prediction, or we would have SSE offset predicted in the results. Next, the overlapping windows provide 10 predictions of noise for each node at every time step. We subtract this noise prediction from the original signal, giving us 10 denoised signals for each time step. The denoised signals are then combined with a simple averaging to produce the result. We tested different aggregation methods such as the average of only the central points of the window, the average after removing extremes, and only using the central point, but there were no obvious differences in the results. This averaging over the overlapping windows enhances stability and precision by mitigating the edge effect of working with time windows. The predicted outcomes are then rescaled, and to offer a complete analysis, the trend is reintroduced to the results, ensuring the incorporation of both short-term predictive patterns and the underlying temporal trend.

## 2.7 Performance metrics

The first metric we consider when evaluating denoising performance is the average position of the entire network. To define this formally we begin by noting that the position of an individual station  $k$  at epoch  $i$  is defined as the change in north, east, and vertical (n,e,u) coordinates with respect to an initial epoch:

$$\Delta \bar{x}_i^k = (n, e, u)_i^k - (n, e, u)_0^k \quad (1)$$

This position is determined on the detrended time series as defined in Section 2.2. Then the position of the entire network at epoch  $i$  is the average over  $N$  stations such that

$$\rho(n, e, u)_i = \frac{1}{N} \sum_{k=1}^N \Delta \bar{x}_i^k \quad (2)$$

The detrended time series is strategically centered around zero along the time axis for each station, ensuring a standardized baseline. Ideally, at any given time-step the average position across the entire network should be zero, as the stations are not anticipated to move uniformly. As such, the average network position at a specific time step provides insight into correlated displacements. With the extensive spatial coverage of the network, stretching eastward by 400 km, even the most substantial SSEs are not expected to exert an influence on the average network position beyond a fraction of a millimeter. This metric is ideal for measuring quantitatively the denoising to a certain level since it is all based on the assumption that there is no noise, all stations should be close to 0 mm on all channels with some random white noise, conserving the network average close to 0 mm. But there are some examples where the network is affected by two spatial patches of noise that cancel each other: the network average position is close to 0 mm, but there are still two patches of common mode noise. We provide an example of this case in Section 3.4 and Figure 9. Therefore, we are using this metric for extreme cases where the entire network is affected, but measuring denoising in specific parts of the network is not possible with this method.

The second metric is the consistency of SSE offsets before and after denoising. To compute these, we first identify SSEs by considering time periods that contain high tremor counts. By plotting those tremors, we can infer the spatial extent of the SSE, and we then select stations within this footprint and period. Then, to measure the SSE offset on the detrended time series, the average position is calculated for the ten days preceding and following each event, at each station as this time window captures the station position before and after the SSE. We compared these offset metrics with and without denoising each SSE with the idea that the two should be similar with and without denoising. We relied heavily on this metric to fine-tune the edge length in the input graphs: short edge lengths allow for a better prediction of local noise, but the SSE offset was also removed, showing only a small residual offset in the denoised data. Edges that are too long do not allow the GNN to capture local noise patterns. We decided to stop increasing the edge length when we maximized the consistency of the SSE offset before and after denoising.

## 2.8 Stack filtering methods

In order to compare our denoising method to a non-machine learning approach, we decided to implement three versions of stack filtering for removing common mode noise. First, we implemented the stack filtering proposed in [Wdowinski et al. \(1997\)](#). This method was applied to a small set of stations surrounding the 1992 Landers earthquake, with the goal of highlighting the differences between stations during and after the earthquake. In this approach, common mode noise is calculated by averaging the time series for all sites, at each time step, resulting in one noise estimate for the full network at each time step, that is then subtracted from the original time series at each station.

The second approach is an extension of this first one, where the common mode noise is calculated by averaging the time series across all stations respecting a certain criterion to prevent including signal of interest in this noise estimation. In our case, we decided to exclude all stations within a 50 km radius of tremors from the stack. Since tremor is spatially correlated with SSEs ([Bartlow et al., 2011](#)) using this proxy allows us to exclude SSE related displacements in the noise estimate. Similar technique has been used recently to remove common mode noise from GNSS time series to study large earthquake precursors ([Bradley and Hubbard, 2023; Bletry and Nocquet, 2025](#)). In those studies, the authors exclude stations within a certain distance of the epicenter of the earthquake of interest.

Finally, we apply a different version of the stack filtering where we calculate a noise estimate for each station by stacking only stations further than a distance threshold compared to the target station. To align with the GNN method, we calculate the average displacement recorded at stations greater than 400 km from the target station. This gives a common mode noise estimate specific to each station.

## 3 Results

### 3.1 Denoising Common Mode Noise

To demonstrate the performance of the GNN denoising we applied the GNN during a time when strong common mode noise was recorded across the Pacific Northwest. The results are shown in Figure 4. In the raw data (Figure 4a), common mode noise manifests as widespread spatial correlation in station displacements across a large area while in the denoised data (Figures 4b-e), these strong trends are removed and there is more variability in GNSS displacements across the network. The table (Figure 4f) shows the average position of the network for each panel. We can see the network offset is greatly reduced for all denoising methods.

Figure 5 shows the time series of the average detrended position of the network for raw and denoised data on the eastern component for the UNR and CWU datasets, for all the denoising methods (methodology described in Section 2.7, the results for the other components are available in the supplementary materials). In Figure 5, the raw detrended data has maximum amplitudes of more than 4 mm on the horizontal compo-

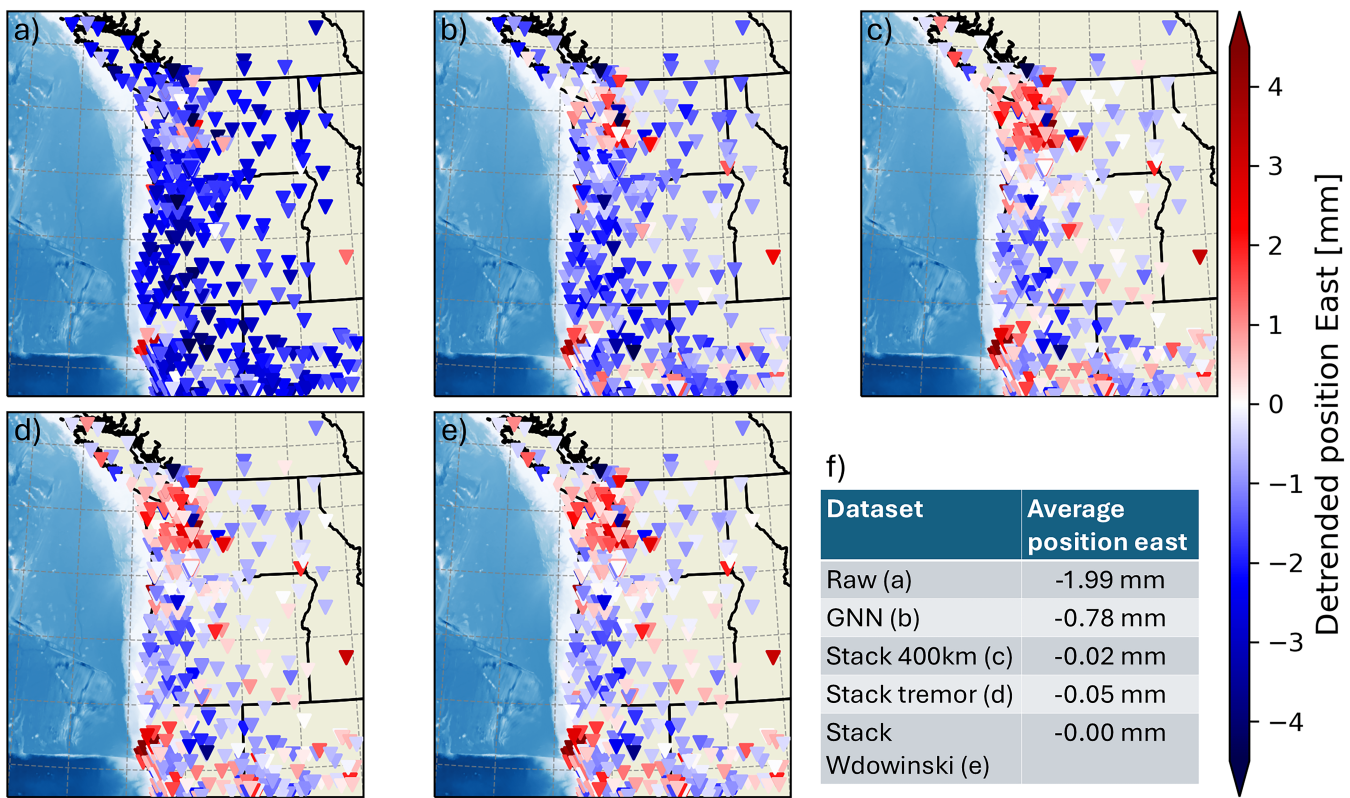


**Figure 4** Comparison of raw and denoised east displacements between the different denoising techniques on April 14, 2010. Each station location is indicated with a triangle color-coded by the eastward displacement. The raw data is in panel a, and panels b-e show the denoised data with the different techniques. Table in f shows the average network position for each panel.

ments recorded by UNR while the CWU amplitudes are only  $\sim 1$  mm. After denoising, the overall amplitudes are significantly reduced in all time series.

To compare Figures 4 and 5, in Figure 4a, the overall network position in the raw detrended data is shifted significantly due to common mode noise, the average network position on the eastern component is -1.99 mm. In the time series shown in Figure 5, the raw detrended data regularly exceed this threshold for the UNR dataset (Figure 5a, c, e, g). Denoising recenters the network for the same day resulting in an average position of only -0.78 mm offset for the GNN denoising as shown in Figure 4b. For reference, on average, the UNR dataset has an offset of 1.083 mm on the eastern component.

We calculated the relative denoising efficacy compared to the original data by calculating the difference in noise level before and after denoising, divided by original noise level. We did so for each component (East, North, and vertical). For the UNR dataset, the GNN reduces noise amplitudes by more than 74% on all components. The stacking methods outperform the GNN with Wdowinski filtering at 100% noise reduction (the method itself is intended to remove what is considered noise in this metric), and the other stacking at more than 95% noise reduction. Both Wdowinski and the tremor stacking method calculate one average position of the network before subtracting it so the performance of these two algorithms is expected. As explained in Section 2.7, the results based on this met-

ric are to be taken with consideration that there is no way to differentiate good common mode noise removal from local common mode noise having cancelling effects. The absolute difference in average position of the network between all methods is only 0.283 mm on the horizontal component, and the maximum average offset is reduced from 4.85 mm to 1.45 mm on the horizontal components for the GNN and down to 0.25 mm for the tremor and 400 km stacking. We also applied these methods to the CWU dataset, that has significantly smaller amplitudes in the raw detrended data. The denoising, for all methods, brings the CWU average network position to the same absolute levels as the denoising UNR dataset (Fig 5b, d, f, h). A summary of the overall denoising performance is shown in supplementary material, Tables 1, 2, 3 and 4, which lists the average and maximum offsets on all components prior to and after GNN denoising, and the three stack filtering. Since the raw detrended data delivered by UNR and CWU have significantly different amplitudes on the horizontals, we also report the offset reduction as a percentage of the raw detrended data amplitude. An interesting observation from comparing the two datasets is regardless of the denoising method, the denoised time series of both datasets have very close maximum offsets.

### 3.2 In-depth analysis of the 2016 SSE

To explore whether denoising can improve geodetic observations of SSEs, we focus on a large magnitude SSE that took place between December 2015 and January

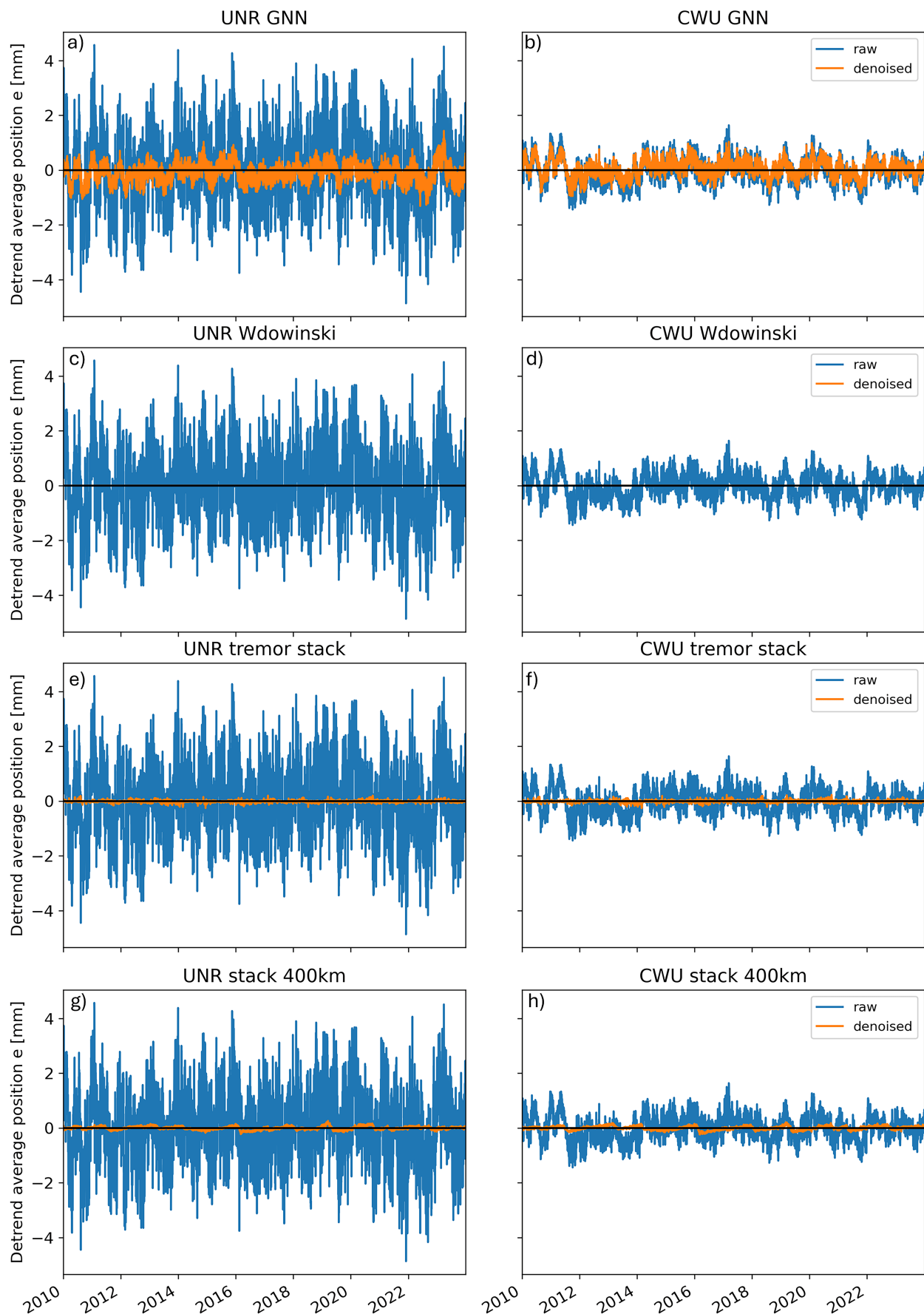


**Figure 5** Time series of the average detrended position of the network on the east component only (other components are available in supplementary material) for the UNR dataset on the left, and the CWU on the right. The raw detrended data is shown in blue and the denoised data is shown in orange. Each row is a different denoising technique (described in Section 2.7). For panels c and d, denoising using Wdowinski's method removes the average position so the result is zero.

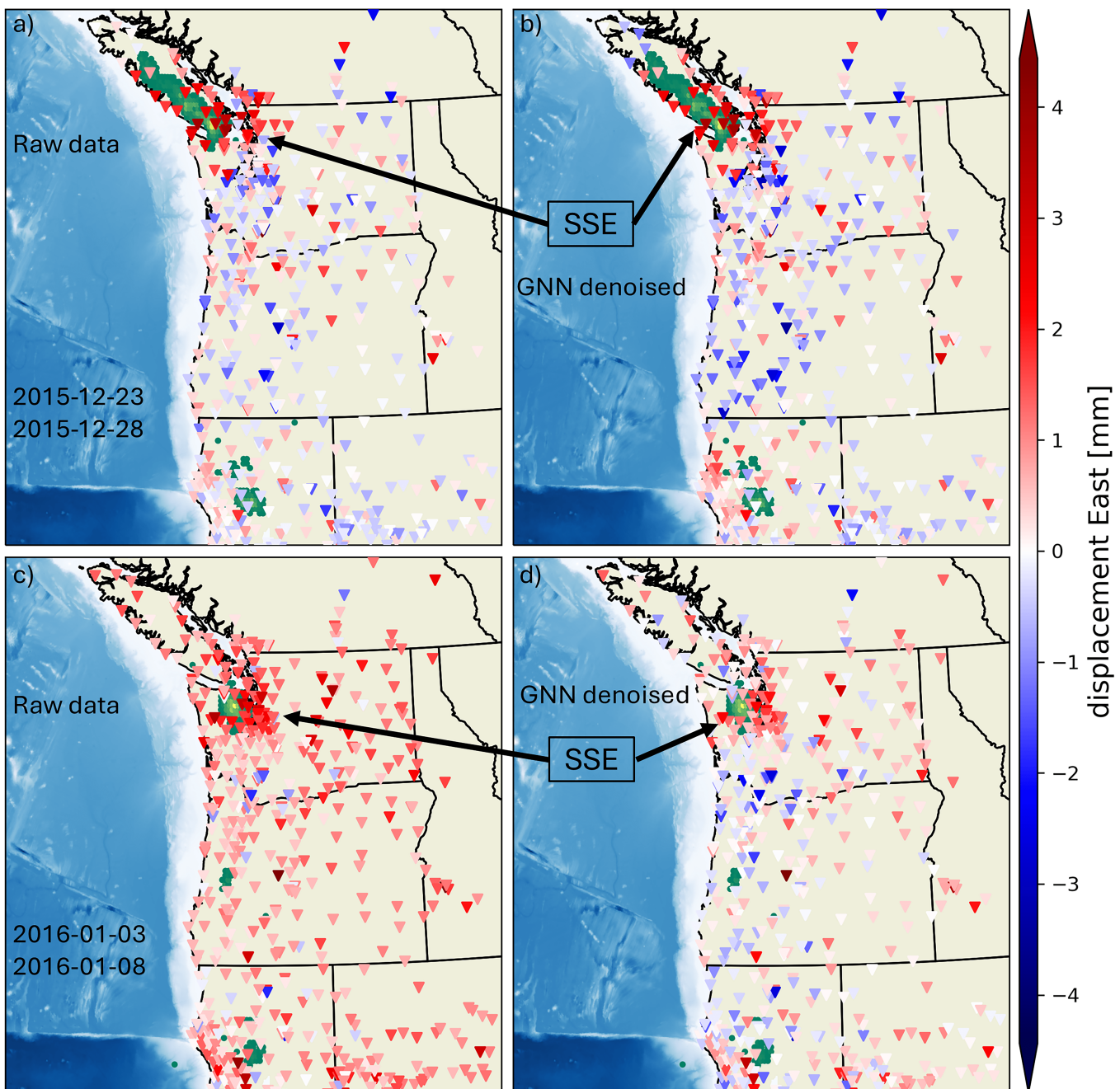


**Figure 6** Raw and denoised GNSS displacements from the 2015–2016 winter slow slip event that extended from Vancouver Island to Puget Sound. Panels a and b show six days of displacement on the eastern component recorded between 2015-12-23 and 2015-12-28. During this time period both the raw (a) and denoised (b) data are similar (i.e. the denoising has little effect) and we observe eastward slip on Vancouver Island owing to the SSE. Panels c and d show six days of displacement during a different, slightly later time period, 2016-01-03 and 2016-01-08, as the slip migrated to the east of the Olympic peninsula. The slip is difficult to see on the raw data (c) due to common mode error shifting the full network in the same direction.

2016. This SSE slipped across an extensive region, beginning in Vancouver Island, and migrated south to the Puget Sound area. Michel et al. (2019) estimates a moment magnitude of 6.79 for this event. The displacement maps for the eastern component reveal significant surface displacements on Vancouver Island between December 23, 2015, and December 28, 2016 (Figure 6a and b), evident in both raw and denoised data and collocated with the tremors. During this time period, the denoised data remains unaltered, affirming the reliability of the denoising process (i.e. denoising does

not remove the signal of interest). In the latter part of this SSE, between January 3 and January 8, 2016, slip migrated to the eastern part of the Olympic Peninsula but the network also experienced a period of strong common mode noise that manifests as eastward displacements across the entire network (Figure 6c). During this period in the raw data, the displacement is nearly imperceptible due to noise. The full network's apparent shift in the same direction as the expected surface displacement masks the underlying motions of stations due to the SSE. After denoising, this common mode sig-

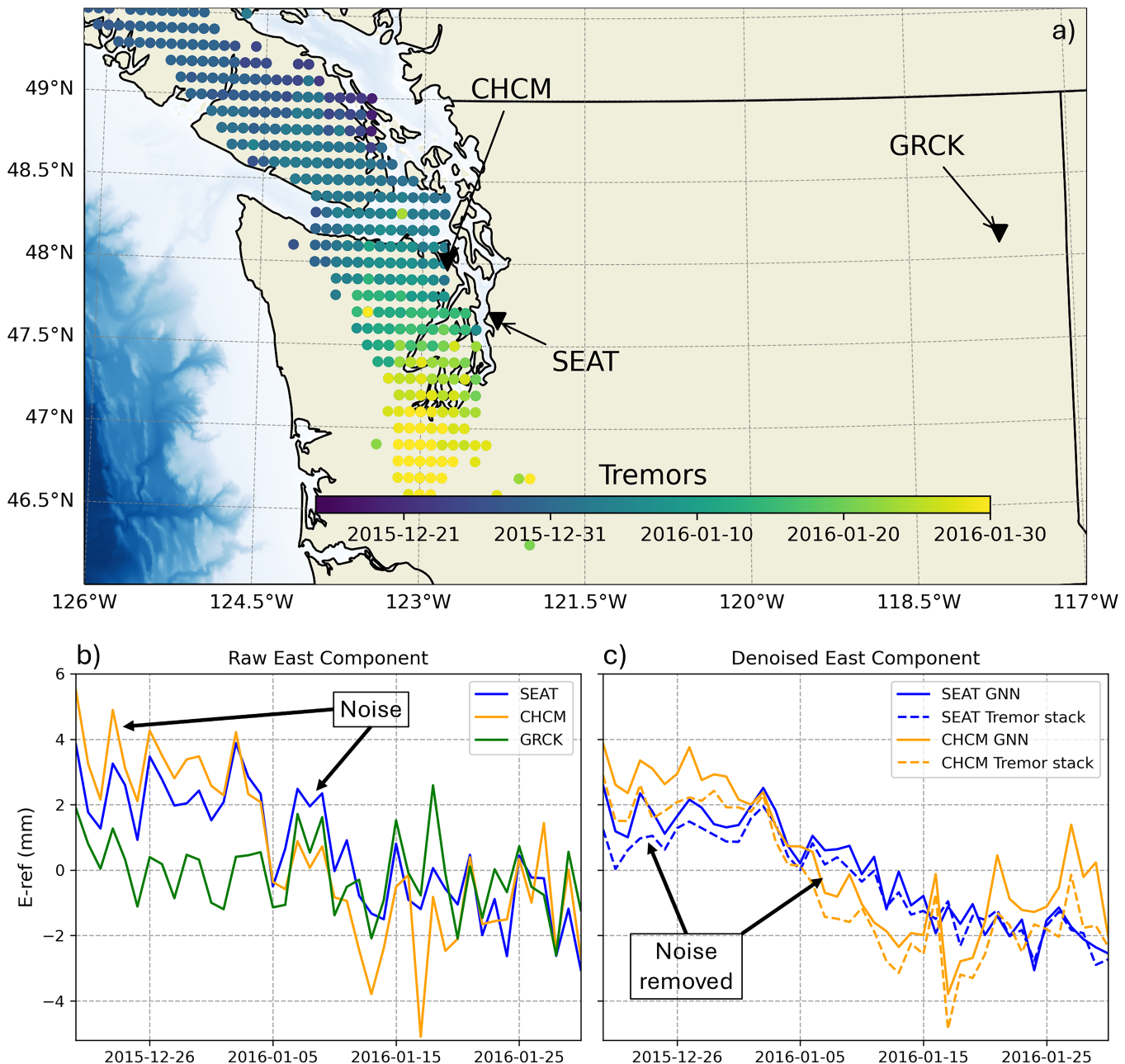


**Figure 7** : Displacements recorded at stations SEAT, CHCM, and GRCK during the 2016 SSE. Panel a) shows the location of two stations that recorded the SSE (SEAT and CHCM), and one station on the east side of the Cascade Range that did not record the SSE (GRCK). Tremor locations are shown as circles color coded by time. Panel b) shows the raw time series recorded on the east component for the three stations. We annotate the timing of common mode error recorded on the three stations. Panel c) shows the same timeseries after denoising with the GNN and the tremor stack; the common mode noise has been removed.

nal is removed greatly reducing the average network offset and facilitating interpretation of surface displacement signals.

To demonstrate denoising capabilities, we selected three stations for further analysis of this event. The first two stations, CHCM and SEAT, are within the footprint of the surface projection of the SSE (i.e. they are surrounded by tremors) and on the eastern edge of the event, respectively. Station GRCK is located 380 km to the east, close to Spokane, WA on the east side of the Cascades. The time series of raw data on January 7, 2016, reveals a common “bump” in all three sta-

tions, including the distant GRCK station, likely caused by common mode noise. If interpreted directly, this artifact indicates that the displacement occurred in three steps: initial westward slip between the 3rd and the 5th of January, followed by a time period of eastward displacement before resuming westward displacement on the 9th. Denoising eliminates the influence of common mode noise, resulting in a smoother signal for the SSE which occurred over a few days. The overall offset remains unchanged but the pattern and therefore the daily velocity during the SSE changes, emphasizing the importance of denoising techniques for an accurate

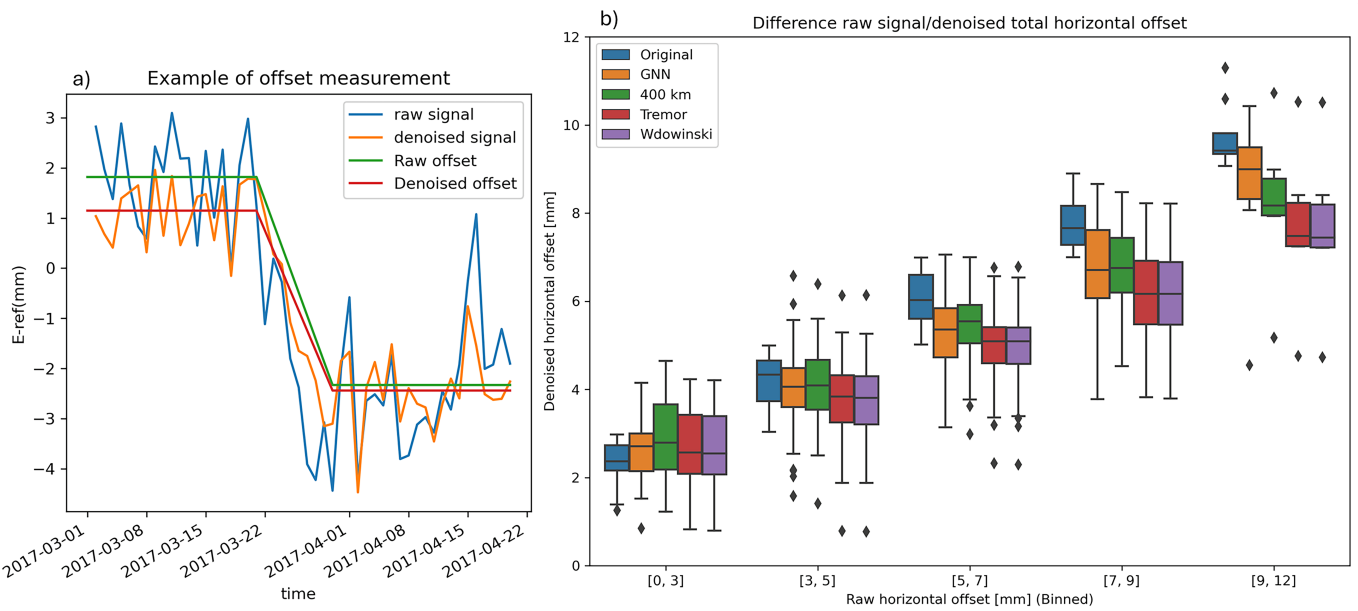


**Figure 8** Comparison of SSE offsets measured on raw and denoised data. Panel a shows an example of SSE offset measurement on the east component at one station. Panel b illustrates the comparison between the different denoising methods and raw horizontal offsets, binned by raw offset. The black diamonds represent the outliers.

representation of SSE dynamics. In Figure 7c, we also show the difference between the GNN denoising and the tremor stacking method. We can see there is no big difference between the two and both remove effectively the common mode noise artifact.

### 3.3 SSE offset consistency

To explore the effect of denoising on SSE surface displacements, we selected a total of 15 events between 2010 and 2023, including events throughout Cascadia (i.e. SSEs from Oregon and northern California). For each of these events, we select stations that visibly recorded displacements and estimate their total offsets on the horizontal components (explained in Section 2.7). To make these measurements, we average the station position over ten days before the start of the SSE and ten days after the termination of the SSE using tremor to determine event start and end times (as shown in Figure 8a). We then use these values to calculate total horizontal offset. We applied this procedure to measure a total of 280 offsets in both raw and denoised time series to evaluate the influence of denoising on SSE offset estimates.

In Figure 8b, we compare offsets estimated from raw timeseries to those estimated from denoised timeseries. We binned the offset measurements by raw offset to compare between denoising techniques. From this, we observe that denoising predominantly maintains the offset of the SSE. However, there is a discernible trend where smaller offsets become slightly amplified after denoising (e.g. in the [0,3] bin in Figure 8b, the original signal has smaller offset than the denoised offset), whereas larger offsets are slightly reduced in amplitude after denoising. Hence, the denoising process introduces subtle adjustments to the offsets. We can also note differences in estimated offsets between denoising techniques, with the GNN performing the best to con-

serve the SSE offset for bigger events compared to other methods. Because it removes the average and does not exclude stations that record SSE offsets, the Wdowinski method removes the most signal because the noise estimate includes contributions from the SSE. Owing to the large extent of the network this correction is <2 mm for the biggest offsets. Interestingly, there is little difference between the tremor stacking and the Wdowinski stacking. This can be explained by the set choice of 50 km radius of tremors for excluding stations from the stack, where for bigger event the effects of SSEs might be visible on GNSS signal further than this threshold. Therefore, the use of tremors to exclude stations might need more fine tuning for each event.

### 3.4 Network size and spatial extent sensitivity

Here we compare the results of the GNN denoising to the 400 km stack filtering detailed in Section 2.8. The 400 km stack filtering is more effective at removing the average offset for our study area: 95% on the horizontal components compared to 75% for the GNN on the UNR dataset. Additionally, the SSE offset results are consistent between the two approaches. This suggests only a marginal benefit between using a more complex machine learning method when compared to the simpler stack filtering. However, there are some benefits to the GNN approach. One important difference is the performance for more localized noise patches. As explained in Section 2.7, if we have two oppositely signed common mode noise patches with approximately the same number of stations sampling both, using the Wdowinski stacking, and the tremor stacking will result in the noise estimate being close to zero and no noise will be removed. Similarly, with this situation, the 400 km stack filtering can actually add noise to the original time series by averaging stations that sample uniform noise.

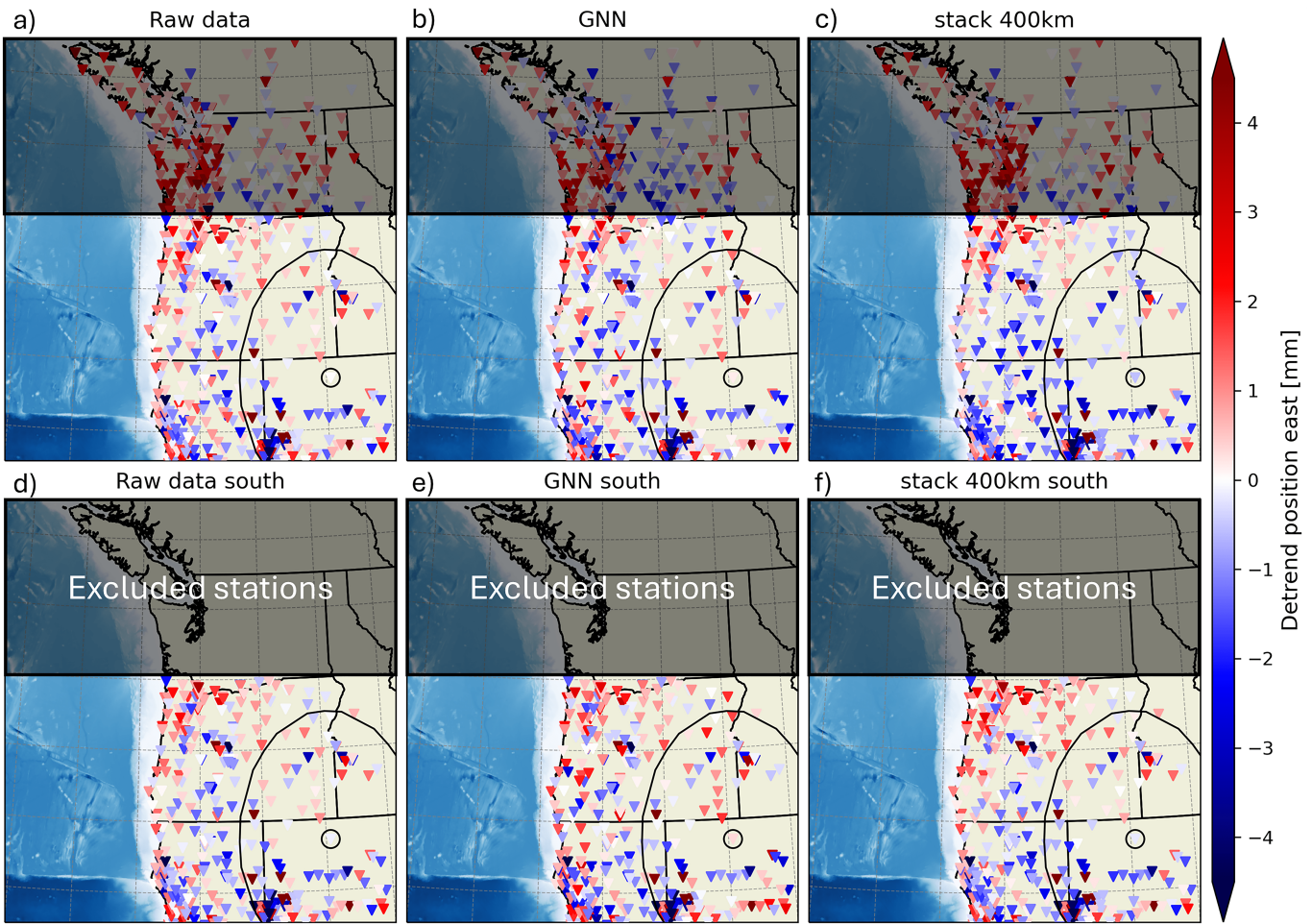


**Figure 9** Denoising comparison between the baseline method and the GNN. Panel a is the raw detrended position on the eastern component; panels b and e are the GNN; and c and f are the Baseline method. The small circle is the location of an example station P013, and the wider circle is the 400 km radius for the mean position calculations.

Figure 9a shows the raw east displacement recorded at each station in Cascadia. During this period, southwestern Cascadia has a small overall westward displacement while northern Cascadia has a larger amplitude, dominantly eastern displacement, both resulting from common mode noise. For a target station in southeastern Cascadia, stacking the stations at a distance greater than 400 km away results in a net eastward displacement. Subtracting this noise estimate does not remove but rather amplifies the noise in southwestern Cascadia. More specifically, looking at station P013 in this example, the raw detrended position on the eastern component is -0.11 mm, while it is -0.64 mm for the baseline denoising and -0.06 mm for the GNN denoising. This station does not seem to be impacted by common mode noise at this time, but since the northern region is, stack filtering adds an additional 0.53 mm westward offset. In contrast, the GNN method captures more of the local noise characteristics and overall has better denoising performance.

Now, if we change the spatial extent of the network to only southern Cascadia (Figure 9 d-f), we can see the results are very different for the 400 km stack filtering solution, where the GNN's results are consistent with the full network. This example shows the importance of careful consideration of the spatial extent of the net-

work and structure of the noise for the stacking methods.

## 4 Discussion

We have demonstrated that GNNs are a promising tool for denoising GNSS time series. They have several attributes that are advantageous for application to geospatial data. For example, unlike other commonly employed single station denoising techniques (e.g., Thomas et al., 2023), GNNs leverage correlated spatial information to make predictions. They are also more resilient to changes in conditions of the observation networks, for instance, they can accommodate spatially heterogeneous station distributions, and varying numbers of available stations (for example during outages), as well as temporal gaps. This capability makes them very appealing for application to GNSS networks for which conditions change greatly over time. Additionally, adding new stations to a pretrained GNN does not require retraining. This flexibility is an advantage compared to more traditional GNSS denoising techniques such as the PCA approach, which requires a fixed set of stations with no data gaps (He et al., 2015; Li et al., 2017).

All methods presented in this study excel at identifying common mode noise recorded across the network.

As shown in Section 3.1, the average horizontal offset of the UNR and CWU networks is reduced by 70% and 30% respectively after denoising for the GNN, and more than 95% for the stacking-based methods. This reduction amounts to an average network offset of 0.3 mm for the horizontal component on both datasets. This improvement is substantial and could facilitate the identification of small magnitude displacements that are typically hidden in the noise.

In general, the simple stack filtering methods can outperform the GNN, while being easy to implement and not requiring training. However, we have also shown that in some cases, stack filtering methods are not robust, even with a network size of over five hundred stations. The differences between methods give them specific strengths and ideal use cases. The classic stack filtering (Wdowinski et al., 1997) was originally developed to highlight differences between stations in the network. This information can be useful for the detection of new SSEs, but as shown in Section 3.3, this method cannot be used to determine absolute offset measurement of SSEs as it incorporates signal in the noise prediction. The tremor-based stacking approach allows for some improvement in this area. The drawback of this method is that it relies on the relationship between tremors and slip, making it impossible to search for small SSEs that might not be accompanied by tremors or for SSEs in locations that do not catalog regularly occurring tremors. Using the 400 km stack filtering for each station solves this issue by not using any other information than the signal itself and the station location. But while showing good performance, this method needs to be employed carefully; as shown in Section 3.4, the results can vary greatly depending on the spatial extent of the network. The GNN, while not showing the best performance on the network average position metric compared to the stacking methods, is the most flexible in terms of network size and spatial extent and is the most general of the four. However, the GNN is also the most complicated method to implement, and the edge length parameter needs to be carefully tuned.

Specific applications of where significant growth of our understanding of geophysical phenomena could occur from meaningful reductions to the noise in GNSS time series are many. For example, precursory phenomena leading up to large ruptures are of interest. Mavrommatis et al. (2014) proposed a long phase of transient deformation potentially associated with deep long-lived slow slip event prior to the M9 Tohoku-oki rupture. Precursory phenomena such as transient deformation in the hours leading up to rupture have also been invoked recently with disputed results (e.g., Bletry and Nocquet, 2025; Hirose et al., 2024). Part of the difficulty in conclusively establishing the existence or absence of these phenomena is that it would have features not unlike common mode noise and the stacking process used to remove these artifacts would also remove the signal. A GNN with suitably long edges would not remove such a slip transient, if it existed, during the denoising process.

More specifically, the example shown in Section 3.2 shows the impact of common mode noise on GNSS

time series. SSEs have complicated dynamics; high-resolution observations of these dynamics provide important constraints on their underlying mechanism. Yet resolving these is a challenge due to the low signal-to-noise ratio which can introduce bias into interpretation. The GNN significantly reduces the noise level, facilitating not only interpretation of dynamics of large SSEs but it may also help identify smaller magnitude SSEs. While the focus of the current study is on SSEs, common mode noise can similarly hinder identification of other tectonic and volcanic processes that result in surface deformation. GNN denoising could also be used to better estimate surface displacements during intermediate magnitude earthquakes as part of early warning systems. Thanks to its flexibility, GNN denoising could be incorporated into any GNSS processing pipelines (like those employed by UNR and CWU). This can extend to real time GNSS which could also benefit from this method as orbits and clocks used in those applications have bigger errors, this is reflected directly in the real time positioning of the stations as correlated noise.

Despite the successes of the GNN, there are still many opportunities to improve GNSS denoising generally. For example, a hybrid approach that uses a GNN to remove spatially correlated noise and single station denoising to remove white noise. These two steps could potentially be combined into one machine learning approach. An additional challenge is that in the absence of ground truth, we cannot quantify the denoising performance in an absolute sense. This is particularly problematic because we may unintentionally remove legitimate signals. Generating synthetic displacement time series using SSE rupture simulations with added noise would be a valuable next step in the verification and enhancement of this method (Costantino et al., 2024). While training with synthetic data offers a clear training target for distinguishing events from noise, it requires accurate simulations to be able to transfer the learning to real world data. If the training dataset is biased, or not perfectly representative of the real-world data, which is likely considering the underlying mechanism of SSEs is still debated, the machine learning model would learn this bias and give inaccurate results.

## 5 Conclusion

Our study demonstrates the efficacy of GNNs in denoising GNSS time series, particularly in handling the spatial heterogeneity and temporal gaps characteristic of evolving GNSS networks. Applying this approach resulted in substantial reduction in common-mode noise, enhancing the precision of surface displacement measurements critical for studying transient deformation signals that are commonly observed in tectonic and volcanic settings. These findings underscore the potential of GNN-based denoising as a robust, adaptive tool for the study of crustal deformation signals. Our study also demonstrates the efficacy of the stack filtering approaches, which each have their strength, and should be considered for their ease of use and efficiency, depending on the application.

## Acknowledgements

We would like to thank the reviewers Hongyu Sun and Walter Szeliga, as well as editor Jonathan Weiss, for their insightful comments that helped us improve the overall quality of the manuscript. This work used the Python programming language (Van Rossum and Drake, 2009), Pytorch and PyTorch Geometric package (Fey and Lenssen, 2019), xarray package (Hoyer and Hamman, 2017). Figures were made with the matplotlib software package (Hunter, 2007). This work is supported by NASA Grants 80NSSC19K0360, 80NSSC19K0741, 80NSSC22K0458, and NSF Cooperative Agreement # 2225286. The authors would also like to thank Daniel Massicotte for his expertise and many productive discussions.

## Data and code availability

The original GNSS time series datasets can be found on the University of Nevada Reno Geodetic Laboratory website (Blewitt et al., 2018), and the EarthScope website for the Central Washington University dataset (Herring et al., 2016). The code to download the data, train the GNN and apply the denoising is available at [https://github.com/UO-Geophysics/daily\\_GNSS\\_denoising](https://github.com/UO-Geophysics/daily_GNSS_denoising) (release v1.0.1, DOI: 10.5281/zenodo.14759013). Additionally, the resulting denoising datasets are available to download on Zenodo (Bachelot, 2024).

## Competing interests

The authors declare no competing interests.

## References

- Azarbad, M. R. and Mosavi, M. R. A new method to mitigate multipath error in single-frequency GPS receiver with wavelet transform. *GPS Solutions*, 18(2):189–198, Mar. 2013. doi: 10.1007/s10291-013-0320-1.
- Bachelot, L. Cascadia GNSS denoised daily time series [Data set], 2024. doi: 10.5281/zenodo.13840584.
- Bartlow, N. M. A Long-Term View of Episodic Tremor and Slip in Cascadia. *Geophysical Research Letters*, 47(3), Feb. 2020. doi: 10.1029/2019gl085303.
- Bartlow, N. M., Miyazaki, S., Bradley, A. M., and Segall, P. Space-time correlation of slip and tremor during the 2009 Cascadia slow slip event. *Geophysical Research Letters*, 38(18), Sept. 2011. doi: 10.1029/2011gl048714.
- Bertiger, W., Bar-Sever, Y., Dorsey, A., Haines, B., Harvey, N., Hemminger, D., Heflin, M., Lu, W., Miller, M., Moore, A. W., Murphy, D., Ries, P., Romans, L., Sibois, A., Sibthorpe, A., Szilagyi, B., Vallisneri, M., and Willis, P. GipsyX/RTGx, a new tool set for space geodetic operations and research. *Advances in Space Research*, 66(3):469–489, Aug. 2020. doi: 10.1016/j.asr.2020.04.015.
- Bletry, Q. and Nocquet, J.-M. Do large earthquakes start with a precursory phase of slow slip? *Seismica*, 3, 2025. doi: 10.26443/seismica.v3i2.1383.
- Bletry, Q., Thomas, A. M., Hawthorne, J. C., Skarbek, R. M., Rempel, A. W., and Krogstad, R. D. Characteristics of secondary slip fronts associated with slow earthquakes in Cascadia. *Earth and Planetary Science Letters*, 463:212–220, Apr. 2017. doi: 10.1016/j.epsl.2017.01.046.
- Blewitt, G., Hammond, W., and Kreemer, C. Harnessing the GPS Data Explosion for Interdisciplinary Science. *Eos*, 99, Sept. 2018. doi: 10.1029/2018eo104623.
- Bloemheuvel, S., van den Hoogen, J., Jozinović, D., Michelini, A., and Atzmueller, M. Graph neural networks for multivariate time series regression with application to seismic data. *International Journal of Data Science and Analytics*, 16(3):317–332, Aug. 2022. doi: 10.1007/s41060-022-00349-6.
- Bock, Y. and Melgar, D. Physical applications of GPS geodesy: a review. *Reports on Progress in Physics*, 79(10):106801, Aug. 2016. doi: 10.1088/0034-4885/79/10/106801.
- Bradley, K. and Hubbard, J. Earthquake precursors? Not so fast. *Earthquake Insights*, July 2023. doi: 10.62481/310cc439.
- Brody, S., Alon, U., and Yahav, E. How Attentive are Graph Attention Networks?, 2021. <https://arxiv.org/abs/2105.14491>. ArXiv.
- Bürgmann, R. The geophysics, geology and mechanics of slow fault slip. *Earth and Planetary Science Letters*, 495:112–134, Aug. 2018. doi: 10.1016/j.epsl.2018.04.062.
- Costantino, G., Giffard-Roisin, S., Mura, M. D., and Socquet, A. Denoising of Geodetic Time Series Using Spatiotemporal Graph Neural Networks: Application to Slow Slip Event Extraction, 2024. doi: 10.48550/ARXIV.2405.03320.
- Delph, J. R., Thomas, A. M., and Levander, A. Subcretionary tectonics: Linking variability in the expression of subduction along the Cascadia forearc. *Earth and Planetary Science Letters*, 556: 116724, Feb. 2021. doi: 10.1016/j.epsl.2020.116724.
- DeMets, C., Gordon, R. G., and Argus, D. F. Geologically current plate motions. *Geophysical Journal International*, 181(1):1–80, Apr. 2010. doi: 10.1111/j.1365-246x.2009.04491.x.
- Dong, D., Fang, P., Bock, Y., Webb, F., Prawirodirdjo, L., Kedar, S., and Jamason, P. Spatiotemporal filtering using principal component analysis and Karhunen-Loeve expansion approaches for regional GPS network analysis. *Journal of Geophysical Research: Solid Earth*, 111(B3), Mar. 2006. doi: 10.1029/2005jb003806.
- Fey, M. and Lenssen, J. E. Fast Graph Representation Learning with PyTorch Geometric, 2019. doi: 10.48550/ARXIV.1903.02428.
- Geng, J., Pan, Y., Li, X., Guo, J., Liu, J., Chen, X., and Zhang, Y. Noise Characteristics of High-Rate Multi-GNSS for Subdaily Crustal Deformation Monitoring. *Journal of Geophysical Research: Solid Earth*, 123(2):1987–2002, Feb. 2018. doi: 10.1002/2018jb015527.
- Geng, J., Chen, X., Pan, Y., Mao, S., Li, C., Zhou, J., and Zhang, K. PRIDE PPP-AR: an open-source software for GPS PPP ambiguity resolution. *GPS Solutions*, 23(4), July 2019. doi: 10.1007/s10291-019-0888-1.
- Ghosh, A., Vidale, J. E., Sweet, J. R., Creager, K. C., Wech, A. G., Houston, H., and Brodsky, E. E. Rapid, continuous streaking of tremor in Cascadia. *Geochemistry, Geophysics, Geosystems*, 11(12), Dec. 2010. doi: 10.1029/2010gc003305.
- Goldberg, D. E. and Haynie, K. L. Ready for Real Time: Performance of Global Navigation Satellite System in 2019 Mw 7.1 Ridgecrest, California, Rapid Response Products. *Seismological Research Letters*, 93(2A):517–530, Jan. 2022. doi: 10.1785/0220210278.
- Hadas, T., Kaplon, J., Bosy, J., Sierny, J., and Wilgan, K. Near-real-time regional troposphere models for the GNSS precise point positioning technique. *Measurement Science and Technology*, 24(5):055003, Mar. 2013. doi: 10.1088/0957-0233/24/5/055003.
- Hawthorne, J. C., Bostock, M. G., Royer, A. A., and Thomas, A. M. Variations in slow slip moment rate associated with rapid tremor reversals in Cascadia. *Geochemistry, Geophysics, Geosystems*, 17(12):4899–4919, Dec. 2016. doi: 10.1002/2016gc006489.

- He, X., Hua, X., Yu, K., Xuan, W., Lu, T., Zhang, W., and Chen, X. Accuracy enhancement of GPS time series using principal component analysis and block spatial filtering. *Advances in Space Research*, 55(5):1316–1327, Mar. 2015. doi: 10.1016/j.asr.2014.12.016.
- Herring, T. A., Melbourne, T. I., Murray, M. H., Floyd, M. A., Szeliga, W. M., King, R. W., Phillips, D. A., Puskas, C. M., Santillan, M., and Wang, L. Plate Boundary Observatory and related networks: GPS data analysis methods and geodetic products. *Reviews of Geophysics*, 54(4):759–808, Oct. 2016. doi: 10.1002/2016rg000529.
- Hirose, H., Kato, A., and Kimura, T. Did Short-Term Preseismic Crustal Deformation Precede the 2011 Great Tohoku-Oki Earthquake? An Examination of Stacked Tilt Records. *Geophysical Research Letters*, 51(12), June 2024. doi: 10.1029/2024gl109384.
- Houston, H., Delbridge, B. G., Wech, A. G., and Creager, K. C. Rapid tremor reversals in Cascadia generated by a weakened plate interface. *Nature Geoscience*, 4(6):404–409, May 2011. doi: 10.1038/ngeo1157.
- Hoyer, S. and Hamman, J. xarray: N-D labeled Arrays and Datasets in Python. *Journal of Open Research Software*, 5(1):10, Apr. 2017. doi: 10.5334/jors.148.
- Hunter, J. D. Matplotlib: A 2D Graphics Environment. *Computing in Science & Engineering*, 9(3):90–95, 2007. doi: 10.1109/mcse.2007.55.
- Ito, Y., Hino, R., Kido, M., Fujimoto, H., Osada, Y., Inazu, D., Ohta, Y., Iinuma, T., Ohzono, M., Miura, S., Mishina, M., Suzuki, K., Tsuji, T., and Ashi, J. Episodic slow slip events in the Japan subduction zone before the 2011 Tohoku-Oki earthquake. *Tectonophysics*, 600:14–26, July 2013. doi: 10.1016/j.tecto.2012.08.022.
- Itoh, Y., Aoki, Y., and Fukuda, J. Imaging evolution of Cascadia slow-slip event using high-rate GPS. *Scientific Reports*, 12(1), May 2022. doi: 10.1038/s41598-022-10957-8.
- Jolivet, R. and Frank, W. B. The Transient and Intermittent Nature of Slow Slip. *AGU Advances*, 1(1), Mar. 2020. doi: 10.1029/2019av000126.
- Kato, A., Obara, K., Igarashi, T., Tsuruoka, H., Nakagawa, S., and Hirata, N. Propagation of Slow Slip Leading Up to the 2011 Mw 9.0 Tohoku-Oki Earthquake. *Science*, 335(6069):705–708, Feb. 2012. doi: 10.1126/science.1215141.
- Kazmierski, K., Zajdel, R., and Sośnica, K. Evolution of orbit and clock quality for real-time multi-GNSS solutions. *GPS Solutions*, 24(4), Aug. 2020. doi: 10.1007/s10291-020-01026-6.
- Kipf, T. and Welling, M. Semi-Supervised Classification with Graph Convolutional Networks, 2017. <http://arxiv.org/abs/1609.02907>. arXiv:1609.02907.
- Kreemer, C., Blewitt, G., and Klein, E. C. A geodetic plate motion and Global Strain Rate Model. *Geochemistry, Geophysics, Geosystems*, 15(10):3849–3889, Oct. 2014. doi: 10.1002/2014gc005407.
- Larson, K. M. Unanticipated Uses of the Global Positioning System. *Annual Review of Earth and Planetary Sciences*, 47(1):19–40, May 2019. doi: 10.1146/annurev-earth-053018-060203.
- Lecun, Y., Bottou, L., Bengio, Y., and Haffner, P. Gradient-based learning applied to document recognition. *Proceedings of the IEEE*, 86(11):2278–2324, 1998. doi: 10.1109/5.726791.
- LeCun, Y., Bengio, Y., and Hinton, G. Deep learning. *Nature*, 521 (7553):436–444, May 2015. doi: 10.1038/nature14539.
- Li, Y., Xu, C., Yi, L., and Fang, R. A data-driven approach for denoising GNSS position time series. *Journal of Geodesy*, 92(8): 905–922, Dec. 2017. doi: 10.1007/s00190-017-1102-2.
- Li, Y., Han, L., Yi, L., Zhong, S., and Chen, C. Feature extraction and improved denoising method for nonlinear and nonstationary high-rate GNSS coseismic displacements applied to earthquake focal mechanism inversion of the El Mayor-Cucapah earthquake. *Advances in Space Research*, 68(10):3971–3991, Nov. 2021. doi: 10.1016/j.asr.2021.07.032.
- Li, Y., Han, L., and Liu, X. Accuracy Enhancement and Feature Extraction for GNSS Daily Time Series Using Adaptive CEEMD-Multi-PCA-Based Filter. *Remote Sensing*, 15(7):1902, Apr. 2023. doi: 10.3390/rs15071902.
- Lin, J., Melgar, D., Thomas, A. M., and Searcy, J. Early Warning for Great Earthquakes From Characterization of Crustal Deformation Patterns With Deep Learning. *Journal of Geophysical Research: Solid Earth*, 126(10), Oct. 2021. doi: 10.1029/2021jb022703.
- Lu, C., Li, X., Li, Z., Heinkelmann, R., Nilsson, T., Dick, G., Ge, M., and Schuh, H. GNSS tropospheric gradients with high temporal resolution and their effect on precise positioning. *Journal of Geophysical Research: Atmospheres*, 121(2):912–930, Jan. 2016. doi: 10.1002/2015jd024255.
- Mavrommatis, A. P., Segall, P., and Johnson, K. M. A decadal-scale deformation transient prior to the 2011 Mw 9.0 Tohoku-oki earthquake. *Geophysical Research Letters*, 41(13):4486–4494, July 2014. doi: 10.1002/2014gl060139.
- McBrearty, I. W. and Beroza, G. C. Earthquake Phase Association with Graph Neural Networks. *Bulletin of the Seismological Society of America*, 113(2):524–547, Jan. 2023. doi: 10.1785/0120220182.
- Meade, B. J. and Hager, B. H. Block models of crustal motion in southern California constrained by GPS measurements. *Journal of Geophysical Research: Solid Earth*, 110(B3), Mar. 2005. doi: 10.1029/2004jb003209.
- Melgar, D., Crowell, B. W., Melbourne, T. I., Szeliga, W., Santillan, M., and Scrivner, C. Noise Characteristics of Operational Real-Time High-Rate GNSS Positions in a Large Aperture Network. *Journal of Geophysical Research: Solid Earth*, 125(7), June 2020. doi: 10.1029/2019jb019197.
- Michel, S., Gualandi, A., and Avouac, J.-P. Similar scaling laws for earthquakes and Cascadia slow-slip events. *Nature*, 574(7779): 522–526, Oct. 2019. doi: 10.1038/s41586-019-1673-6.
- Miller, M. M., Melbourne, T., Johnson, D. J., and Sumner, W. Q. Periodic Slow Earthquakes from the Cascadia Subduction Zone. *Science*, 295(5564):2423–2423, Mar. 2002. doi: 10.1126/science.1071193.
- Moreno, M., Melnick, D., Rosenau, M., Bolte, J., Klotz, J., Echtler, H., Baez, J., Bataille, K., Chen, J., Bevis, M., Hase, H., and Oncken, O. Heterogeneous plate locking in the South-Central Chile subduction zone: Building up the next great earthquake. *Earth and Planetary Science Letters*, 305(3–4):413–424, May 2011. doi: 10.1016/j.epsl.2011.03.025.
- Nikolaidis, R. Observation of Geodetic and Seismic Deformation with the Global Positioning System, 2002.
- Nishimura, T., Matsuzawa, T., and Obara, K. Detection of short-term slow slip events along the Nankai Trough, southwest Japan, using GNSS data. *Journal of Geophysical Research: Solid Earth*, 118 (6):3112–3125, June 2013. doi: 10.1002/jgrb.50222.
- Peng, Y., Rubin, A. M., Bostock, M. G., and Armbruster, J. G. High-resolution imaging of rapid tremor migrations beneath southern Vancouver Island using cross-station cross correlations. *Journal of Geophysical Research: Solid Earth*, 120(6):4317–4332, June 2015. doi: 10.1002/2015jb011892.
- Prawirodirdjo, L. and Bock, Y. Instantaneous global plate motion model from 12 years of continuous GPS observations. *Journal of Geophysical Research: Solid Earth*, 109(B8), Aug. 2004. doi: 10.1029/2003jb002944.

- Rogers, G. and Dragert, H. Episodic Tremor and Slip on the Cascadia Subduction Zone: The Chatter of Silent Slip. *Science*, 300 (5627):1942–1943, June 2003. doi: 10.1126/science.1084783.
- Rollins, C. and Avouac, J. A Geodesy- and Seismicity-Based Local Earthquake Likelihood Model for Central Los Angeles. *Geophysical Research Letters*, 46(6):3153–3162, Mar. 2019. doi: 10.1029/2018gl080868.
- Rollins, C., Avouac, J., Landry, W., Argus, D. F., and Barbot, S. Interseismic Strain Accumulation on Faults Beneath Los Angeles, California. *Journal of Geophysical Research: Solid Earth*, 123(8): 7126–7150, Aug. 2018. doi: 10.1029/2017jb015387.
- Ronneberger, O., Fischer, P., and Brox, T. *U-Net: Convolutional Networks for Biomedical Image Segmentation*, page 234–241. Springer International Publishing, 2015. doi: 10.1007/978-3-319-24574-4\_28.
- Royer, A. A., Thomas, A. M., and Bostock, M. G. Tidal modulation and triggering of low-frequency earthquakes in northern Cascadia. *Journal of Geophysical Research: Solid Earth*, 120(1): 384–405, Jan. 2015. doi: 10.1002/2014jb011430.
- Rubin, A. M. and Armbruster, J. G. Imaging slow slip fronts in Cascadia with high precision cross-station tremor locations. *Geochemistry, Geophysics, Geosystems*, 14(12):5371–5392, Dec. 2013. doi: 10.1002/2013gc005031.
- Ruiz, S., Metois, M., Fuenzalida, A., Ruiz, J., Leyton, F., Grandin, R., Vigny, C., Madariaga, R., and Campos, J. Intense foreshocks and a slow slip event preceded the 2014 Iquique Mw 8.1 earthquake. *Science*, 345(6201):1165–1169, Sept. 2014. doi: 10.1126/science.1256074.
- Satirapod, C. and Rizos, C. MULTIPATH MITIGATION BY WAVELET ANALYSIS FOR GPS BASE STATION APPLICATIONS. *Survey Review*, 38(295):2–10, Jan. 2005. doi: 10.1179/sre.2005.38.295.2.
- Shi, Y., Huang, Z., Feng, S., Zhong, H., Wang, W., and Sun, Y. Masked Label Prediction: Unified Message Passing Model for Semi-Supervised Classification, 2021. <http://arxiv.org/abs/2009.03509>. arXiv:2009.03509.
- Socquet, A., Valdes, J. P., Jara, J., Cotton, F., Walpersdorf, A., Cotte, N., Specht, S., Ortega-Culaciati, F., Carrizo, D., and Norabuena, E. An 8 month slow slip event triggers progressive nucleation of the 2014 Chile megathrust. *Geophysical Research Letters*, 44(9): 4046–4053, May 2017. doi: 10.1002/2017gl073023.
- Szeliga, W., Melbourne, T., Santillan, M., and Miller, M. GPS constraints on 34 slow slip events within the Cascadia subduction zone, 1997–2005. *Journal of Geophysical Research: Solid Earth*, 113(B4), Apr. 2008. doi: 10.1029/2007jb004948.
- Tao, Y., Liu, C., Liu, C., Zhao, X., and Hu, H. Empirical Wavelet Transform Method for GNSS Coordinate Series Denoising. *Journal of Geovisualization and Spatial Analysis*, 5(1), Apr. 2021. doi: 10.1007/s41651-021-00078-7.
- Thomas, A., Melgar, D., Dybing, S. N., and Searcy, J. R. Deep learning for denoising High-Rate Global Navigation Satellite System data. *Seismica*, 2(1), May 2023. doi: 10.26443/seismica.v2i1.240.
- van den Ende, M. P. A. and Ampuero, J. Automated Seismic Source Characterization Using Deep Graph Neural Networks. *Geophysical Research Letters*, 47(17), Sept. 2020. doi: 10.1029/2020gl088690.
- Van Rossum, G. and Drake, F. L. *Python 3 Reference Manual*. CreateSpace, Scotts Valley, CA, 2009.
- Wallace, L. M. Slow Slip Events in New Zealand. *Annual Review of Earth and Planetary Sciences*, 48(1):175–203, May 2020. doi: 10.1146/annurev-earth-071719-055104.
- Wang, K., He, J., Dragert, H., and James, T. S. Three-dimensional viscoelastic interseismic deformation model for the Cascadia subduction zone. *Earth, Planets and Space*, 53(4):295–306, 2001. doi: 10.1186/bf03352386.
- Wdowinski, S., Bock, Y., Zhang, J., Fang, P., and Genrich, J. Southern California permanent GPS geodetic array: Spatial filtering of daily positions for estimating coseismic and postseismic displacements induced by the 1992 Landers earthquake. *Journal of Geophysical Research: Solid Earth*, 102(B8):18057–18070, Aug. 1997. doi: 10.1029/97jb01378.
- Wech, A. G. Cataloging Tectonic Tremor Energy Radiation in the Cascadia Subduction Zone. *Journal of Geophysical Research: Solid Earth*, 126(10), Oct. 2021. doi: 10.1029/2021jb022523.
- Wu, X., Hu, X., Wang, G., Zhong, H., and Tang, C. Evaluation of COMPASS ionospheric model in GNSS positioning. *Advances in Space Research*, 51(6):959–968, Mar. 2013. doi: 10.1016/j.asr.2012.09.039.
- Zhang, X., Reichard-Flynn, W., Zhang, M., Hirn, M., and Lin, Y. Spatiotemporal Graph Convolutional Networks for Earthquake Source Characterization. *Journal of Geophysical Research: Solid Earth*, 127(11), Nov. 2022. doi: 10.1029/2022jb024401.
- Zhu, W., Mousavi, S. M., and Beroza, G. C. Seismic Signal Denoising and Decomposition Using Deep Neural Networks. *IEEE Transactions on Geoscience and Remote Sensing*, 57(11):9476–9488, Nov. 2019. doi: 10.1109/tgrs.2019.2926772.

The article *Cascadia Daily GNSS Time Series Denoising: Graph Neural Network and Stack Filtering* © 2025 by L. Bachelder is licensed under CC BY 4.0.